Self-energy matrices for electron transport calculations within the real-space finite-difference formalism

Shigeru Tsukamoto, ^{1,*} Tomoya Ono, ² Kikuji Hirose, ³ and Stefan Blügel ¹

¹Peter Grünberg Institut & Institute for Advanced Simulation, Forschungszentrum Jülich and JARA, D-52425 Jülich, Germany

²Center for Computational Sciences, University of Tsukuba, Tsukuba, Ibaraki 305-8577, Japan

³Graduate School of Engineering, Osaka University, Suita, Osaka 565-0871, Japan

(Received 31 March 2016; revised manuscript received 22 November 2016; published 20 March 2017)

The self-energy term used in transport calculations, which describes the coupling between electrode and transition regions, is able to be evaluated only from a limited number of the propagating and evanescent waves of a bulk electrode. This obviously contributes toward the reduction of the computational expenses in transport calculations. In this paper, we present a mathematical formula for reducing the computational expenses further without using any approximation and without losing accuracy. So far, the self-energy term has been handled as a matrix with the same dimension as the Hamiltonian submatrix representing the interaction between an electrode and a transition region. In this work, through the singular-value decomposition of the submatrix, the self-energy matrix is handled as a smaller matrix, whose dimension is the rank number of the Hamiltonian submatrix. This procedure is practical in the case of using the pseudopotentials in a separable form, and the computational expenses for determining the self-energy matrix are reduced by 90% when employing a code based on the real-space finite-difference formalism and projector-augmented wave method. In addition, this technique is applicable to the transport calculations using atomic or localized basis sets. Adopting the self-energy matrices obtained from this procedure, we present the calculation of the electron transport properties of C₂₀ molecular junctions. The application demonstrates that the electron transmissions are sensitive to the orientation of the molecule with respect to the electrode surface. In addition, channel decomposition of the scattering wave functions reveals that some unoccupied C20 molecular orbitals mainly contribute to the electron conduction through the molecular junction.

DOI: 10.1103/PhysRevE.95.033309

I. INTRODUCTION

Electron transport through nanoscale objects, such as atomic chains, nanowires, quantum point contacts, molecular junctions, and their integrated systems, has been studied since the mid-1990s and is still an active research field of pioneering quantum nanoelectronics and spintronics from the viewpoints of fundamental physics and industrial applications. Further fundamental study on the quantum behavior of electrons flowing through the nanoscale systems motivates us to apply the quantum phenomena toward nanoscale electronic and spintronic devices in the near future. Indeed, the electron transport properties of the nanoscale junction systems have been strenuously investigated from both theoretical and experimental approaches, enabling the accumulation of a large amount of scientific knowledge about electron transport phenomena [1–4].

From a theoretical point of view, various calculation methods for simulating ballistic electron transport phenomena have been proposed and developed. Many of them treat a so-called junction structure, which is composed of a couple of semi-infinite metal electrodes and a scattering body in between. Electron transport studies on such nanoscale junction systems have produced a number of impressive findings and facilitated the understanding of quantum transport phenomena by means of various calculation methods, e.g., those using an electron-scattering quantum-chemistry technique [5], a nonequilibrium Green's function [6–9], a recursion trans-

fer matrix [10], a wave-function-matching scheme [11–15], the Lippmann-Schwinger equation [16], and a wavelet basis set [17]. Nowadays, these calculation methods are required to treat larger and more realistic systems with higher accuracy for profound interpretation of electron transport phenomena and for quantitative comparison to experimental observations.

To meet such demands for accurate electron transport calculations, the coupling interaction between a semi-infinite electrode and a transition region has to be determined accurately. In the electron transport calculations based on the density-functional theory [18], the effective Hamiltonian originating from the coupling interaction is named "selfenergy" [19]. Sørensen et al. proposed a procedure to reduce the computational expenses for determining the self-energy term by excluding rapidly decaying evanescent waves from composing the self-energy matrix [20]. However, the procedure requires increasing the length of the transition region by inserting extra layers so such evanescent components of scattering wave functions decay and become negligible at the interface between the electrode and transition regions [21]. This increases the computational expenses for determining the scattering wave functions in the transition region. In 2016, we proposed an alternative procedure to determine the self-energy matrix accurately only from a limited number of propagating and evanescent (generalized Bloch) waves without increasing the size of the transition region [6]. In this procedure, the self-energy matrix composed of the limited number of the generalized Bloch waves is regularized by adding orthogonal component vectors. The regularized self-energy matrix is refined by having it undergo a self-consistent process [6,12].

^{*}Corresponding author: s.tsukamoto@fz-juelich.de

Although the self-energy matrix handled in these aforementioned procedures is equal in dimensions to the Hamiltonian submatrix representing the interaction between the electrode and transition regions, it can be essentially handled as a smaller matrix when the Hamiltonian submatrix is rank deficient. The reason for this is that the number of the generalized Bloch waves to be involved in the self-energy matrix is not as high as the row and column dimensions of the Hamiltonian submatrix but is only the rank number of the submatrix. Therefore, the self-energy matrix can be represented as a square matrix of the order of its rank number. Such a rank-deficient Hamiltonian submatrix appears, for example, in the case of using pseudopotentials in a separable form, and they are frequently used in modern transport calculations.

In this paper, we present a mathematical formula to handle the self-energy matrix as a smaller matrix and to determine the matrix with lower computational expenses without any approximation and without losing accuracy. Through the singular-value decomposition technique and unitary transformation, the effective Kohn-Sham Hamiltonian submatrix describing the coupling interaction between a semi-infinite electrode and a transition region is reduced in size to a square diagonal matrix of the order of its rank number. Because the dimensions of the self-energy matrix are given as those of the reduced Hamiltonian submatrix, the self-energy term can be handled as a square matrix of the order of the rank number, and, consequently, the computational expenses for determining the self-energy matrix can be reduced. Note that throughout this paper the formulation is presented on the basis of the real-space finite-difference formalism; however, this procedure is also applicable to the transport calculation method using atomic or localized basis sets.

As an application of the self-energy matrices obtained by the present formula, we examine the electron transport properties of molecular junctions composed of a C_{20} fullerene molecule and a couple of fully atomistic crystalline semi-infinite electrodes. The C_{20} molecule is known as the smallest fullerene [22,23] and is expected to work as an electric device component [24,25] like a C_{60} molecule [26]. Nevertheless, the detailed electron transport properties, such as channel-decomposed transmissions and conduction paths in real space, have not been intensively investigated so far. In this paper, in addition to the formulation, we report the electron transport properties of the C_{20} molecular junctions from the viewpoints of transmission channels and their spatial distributions, which are evaluated from scattering wave functions obtained by our method.

The rest of this paper is organized as follows: In Sec. II, we present the detailed formulation to process the rank-deficient submatrices by means of linear-algebraic techniques and how to determine the self-energy matrices. In Sec. III, using our procedure, we demonstrate the calculation of the scattering wave functions for fully atomistic C_{20} molecular junctions and analyze the electron transport properties in detail. In Sec. IV, we summarize the improvements in the mathematical procedure to evaluate the self-energy matrices and its application to the molecular junctions with fully atomistic electrodes. Finally, some mathematical supplemental details are described in the Appendices.

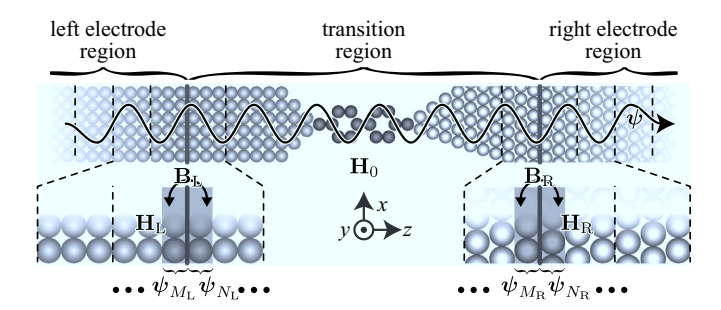


FIG. 1. Schematic representation of a junction system used in electron transport calculations typically. The junction system is partitioned into a transition region and left and right electrode regions by boundary planes represented by the thick lines. The dark gray areas represent the boundary regions, only in which the interaction matrices \mathbf{B}_L and \mathbf{B}_R act on the scattering wave function $\boldsymbol{\psi}$, as seen in Eq. (2). The parts of the scattering wave function $\boldsymbol{\psi}$, which are included in the boundary regions, are denoted by $\boldsymbol{\psi}_{M_L}$, $\boldsymbol{\psi}_{N_L}$, $\boldsymbol{\psi}_{M_R}$, and $\boldsymbol{\psi}_{N_R}$. The matrices \mathbf{H}_0 , \mathbf{H}_L , and \mathbf{H}_R represent the Hamiltonians truncated by the transition region, a unit cell of the left electrode, and a unit cell of the right electrode, respectively.

II. REDUCING DIMENSION OF SELF-CONSISTENT EQUATION

A. Conventional procedure

According to the density-functional theory [18], the behavior of electrons injected from an electrode and scattered in a transition region, as depicted in Fig. 1, is described as a single-particle Kohn-Sham orbital function ψ [27], which satisfies the following Kohn-Sham equation [28,29] in the form of a generalized eigenvalue problem:

$$(\mathbf{H} - \varepsilon \mathbf{S}) \psi = 0, \tag{1}$$

where the eigenvalue ε corresponds to the energy of the scattering electrons. The matrix **H** represents the Hamiltonian of the Kohn-Sham auxiliary system including a pair of semiinfinite electrodes, so the Kohn-Sham matrix equation (1) has an infinite dimension. In the incorporation of modern pseudopotential schemes, such as the projector augmented wave method [30] and the ultrasoft pseudopotential method [31], which relax the norm-conserving condition of conventional pseudopotentials [32], the overlap operator represented by the matrix S is not an identity. However, because of the finite spatial expanse of the nonlocal pseudopotential, the matrix Scan be expressed as a sparse matrix having nonzero elements only at the vicinities of the diagonal line. Hereafter, such sparse matrix (operator) is referred to as a semilocal matrix (operator). For the same reason, the potential operator included in the Hamiltonian matrix **H** is also semilocal. Therefore, these two operators are expressed as band matrices with a bandwidth corresponding to the nonlocal regions of pseudopotentials.

Within the framework of the real-space finite-difference formalism [33], physical quantities are directly represented on discretized real-space grid points. Applying the finite-difference approximation of the formalism on the kinetic energy operator included in the Hamiltonian matrix **H**, it becomes a semilocal linear operator and is also expressed as a band matrix with a bandwidth corresponding to the

approximation order N_f . Consequently, the matrix $\mathbf{H} - \varepsilon \mathbf{S}$ in Eq. (1), which is referred to as Kohn-Sham matrix hereafter, is a band matrix.

Intuitive understanding of the semilocality of the Kohn-Sham matrix $\mathbf{H} - \varepsilon \mathbf{S}$ can be achieved by rewriting Eq. (1) in detail:

\[\cdot \.	· · · ·]			
٠.	\mathbf{C}_{L}	${f B}_{ m L}$	0	0		$m{\psi}_{M_{ m L}}$		
	$\mathbf{B}_{ extsf{L}}^{ ext{T}}$	${f A}_{ m L}$	··. 0	0		$oldsymbol{\psi}_{N_{ m L}}$		
						$\begin{vmatrix} \vdots \\ - \end{vmatrix} = 0$	(2)	
	0	0	\mathbf{C}_{R}	${f B}_{ m R}$		$oldsymbol{\psi}_{M_{\mathrm{R}}}$		
	0	0	$\mathbf{B}_{\mathrm{R}}^{\mathrm{T}}$	${f A}_{ m R}$	·	$m{\psi}_{N_{\mathrm{R}}}$		
				٠. ٠.	٠.]			

Here, only a diagonal block corresponding to the transition region (the submatrix enclosed by the thick lines) and its surrounding blocks are shown, while the Kohn-Sham matrix equation (1) is infinite in the dimension. Hereafter, the vertical and horizontal thick lines in matrices represent boundary planes between the transition region and either electrode region, and they correspond to the vertical thick lines in Fig. 1. Here, we assume each boundary plane to be placed deep enough inside of the electrode so the interaction between the transition and electrode regions is converged to that between neighboring unit cells in the corresponding bulk electrode. Due to the real-space finite-difference formalism, direct interaction between the two electrode regions is represented by zero matrices, and interactions crossing over the left and right boundary planes are expressed by the finite-sized submatrices \mathbf{B}_{L} and \mathbf{B}_{R} (see Fig. 1), which are referred to as left and right interaction matrices hereafter, respectively. Then we define the dimensions of the interaction matrix $\mathbf{B}_{L(R)}$ as $M_{L(R)} \times N_{L(R)}$ and allow them to be rectangular, i.e., $M_{L(R)} \neq N_{L(R)}$. The matrix dimensions $M_{L(R)}$ and $N_{L(R)}$ are determined by the distribution of nonzero elements in the off-diagonal block in Eq. (2). More specifically, they are dominated by the finitedifference approximation order $N_{\rm f}$ and how much nonlocal parts of pseudopotentials stick out from the transition region to the corresponding electrode region in the z direction [34]. Hence, they are given as integer multiples of the number of the grid points in an xy plane (for more details, see Ref. [35]). The subscript L (R) denotes that a quantity with the subscript is associated with the left (right) boundary. The matrices $\mathbf{A}_{L(R)}$ and $\mathbf{C}_{L(R)}$ at the diagonal positions are square submatrices of the Kohn-Sham matrix, the order of which are $N_{L(R)}$ and $M_{L(R)}$, respectively. As seen in Eq. (2), the interaction matrices \mathbf{B}_{L} and \mathbf{B}_{R} and their transposes operate only on limited parts of the scattering wave function vector $\boldsymbol{\psi}$, and we refer to these subvectors as $\boldsymbol{\psi}_{M_{L}}$, $\boldsymbol{\psi}_{N_{L}}$, $\boldsymbol{\psi}_{M_{R}}$, and $\boldsymbol{\psi}_{N_{L}}$. As illustrated in Fig. 1, the subvectors $\boldsymbol{\psi}_{M_{L(R)}}$ and $\boldsymbol{\psi}_{N_{L(R)}}$ are composed of $M_{L(R)}$ and $N_{L(R)}$ elements of the scattering wave-function vector $\boldsymbol{\psi}$, which are contained in the left- and right-side boundary regions of the left (right) boundary plane, respectively (for the boundary regions, see Fig. 1). The effective potentials in the boundary regions can be assumed to be identical to those of the corresponding bulk electrodes.

To solve the Kohn-Sham equation (1) for the scattering wave function ψ , open boundary conditions are applied to the scattering wave function subvectors ψ_{M_L} , ψ_{N_L} , ψ_{M_R} , and ψ_{N_R} so the wave function asymptotically approaches a linear combination of the generalized Bloch wave functions of corresponding bulk electrodes. Now, let us consider a scattering wave function of electrons injected from deep inside of the left electrode, as depicted in Fig. 1. After the incident

wave is scattered in the transition region, a part of the wave is reflected to reach the left electrode, and the other transmits to reach the right one. These reflected and transmitted waves are expressed as linear combinations of reflection and transmission wave components in the left and right boundary regions, respectively. Therefore, the scattering wave functions in the boundary regions are written as

$$\psi_{M_{\mathrm{L}}(N_{\mathrm{L}})} = \phi_{M_{\mathrm{L}}(N_{\mathrm{L}})}^{\mathrm{in}} + \mathbf{Q}_{M_{\mathrm{L}}(N_{\mathrm{L}})}^{\mathrm{ref}} \mathbf{r}$$
 (3)

for the left electrode and

$$\psi_{M_{\mathbf{P}}(N_{\mathbf{P}})} = \mathbf{Q}_{M_{\mathbf{P}}(N_{\mathbf{P}})}^{\text{tra}} t \tag{4}$$

for the right electrode. The vector $\phi_{M_L(N_L)}^{\text{in}}$ denotes the incident electron wave in the left boundary region and is given as one of the rightward propagating Bloch waves in the left bulk electrode. The column vectors composing the matrices $\mathbf{Q}_{M_L(N_L)}^{\text{ref}}$ and $\mathbf{Q}_{M_R(N_R)}^{\text{tra}}$ are given as the left- and right-ward propagating or decaying generalized Bloch waves in the left and right bulk electrodes, respectively [12,13,15]. The vectors \mathbf{r} and \mathbf{t} are composed of the reflection and transmission coefficients of the scattering wave function, respectively.

Kong *et al.* [14] and Egami *et al.* [15] clarified that by applying the open boundary conditions (3) and (4) to the middle block row between the horizontal thick lines in Eq. (2), one can derive the following finite-dimensional Kohn-Sham equation for the scattering wave function in the transition region in the form of linear equations:

$$(\varepsilon \mathbf{S}_{0} - \mathbf{H}_{0} - \boldsymbol{\Sigma}_{0}) \begin{bmatrix} \boldsymbol{\psi}_{N_{L}} \\ \vdots \\ \boldsymbol{\psi}_{M_{P}} \end{bmatrix} = \begin{bmatrix} \mathbf{B}_{L}^{T} \boldsymbol{\phi}_{M_{L}}^{\text{in}} - \boldsymbol{\Sigma}_{L} \boldsymbol{\phi}_{N_{L}}^{\text{in}} \\ 0 \\ \vdots \\ 0 \end{bmatrix}, \quad (5)$$

where the matrices \mathbf{S}_0 and \mathbf{H}_0 are the overlap and Hamiltonian matrix blocks truncated by the transition region, respectively. The matrix $\mathbf{\Sigma}_0$ contains nonzero submatrices $\mathbf{\Sigma}_L$ and $\mathbf{\Sigma}_R$ only at the top-left and bottom-right corners, respectively. The matrices $\mathbf{\Sigma}_L$ and $\mathbf{\Sigma}_R$ represent retarded self-energy operators of the corresponding electrodes and are defined as

$$\mathbf{\Sigma}_{L} = \mathbf{B}_{L}^{T} \mathbf{Q}_{M_{L}}^{\text{ref}} \left[\mathbf{B}_{L} \mathbf{Q}_{N_{L}}^{\text{ref}} \right]^{-1} \mathbf{B}_{L}$$
 (6)

and

$$\mathbf{\Sigma}_{R} = \mathbf{B}_{R} \mathbf{Q}_{N_{R}}^{\text{tra}} \left[\mathbf{B}_{R}^{\text{T}} \mathbf{Q}_{M_{R}}^{\text{tra}} \right]^{-1} \mathbf{B}_{R}^{\text{T}}, \tag{7}$$

respectively [36]. Note that the inverse matrices in the aforementioned equations are, to be exact, pseudoinverse matrices [37,38] and that the self-energy matrix $\Sigma_{L(R)}$ is square of the order $N_L(M_R)$.

In actual computations of the self-energy matrices, calculating all the generalized Bloch waves, i.e., all the column vectors composing the generalized Bloch wave matrices $\mathbf{Q}_{M_{L(R)}}^{\text{ref(tra)}}$ and $\mathbf{Q}_{N_{L(R)}}^{\text{ref(tra)}}$, is impractical, because some generalized Bloch waves are known to decay rapidly and to contain large numerical error, as discussed in Ref. [12]. To overcome the numerical instability and to obtain the self-energy matrices Σ_L and Σ_R accurately, we have so far used a different approach, which solves the following equations for the self-energy matrices Σ_L and Σ_R in a self-consistent manner (for the derivation, see

Appendix A):

$$\Sigma_{L} = \mathbf{B}_{L}^{\mathrm{T}} [\mathbf{G}_{L,BR} + \mathbf{G}_{L,BL} \Sigma_{L} (\mathbf{I}_{N_{L}} - \mathbf{G}_{L,TL} \Sigma_{L})^{-1} \mathbf{G}_{L,TR}] \mathbf{B}_{L},$$
(8)

$$\Sigma_{R} = \mathbf{B}_{R} [\mathbf{G}_{R,TL} + \mathbf{G}_{R,TR} \Sigma_{R} (\mathbf{I}_{M_{R}} - \mathbf{G}_{R,BR} \Sigma_{R})^{-1} \mathbf{G}_{R,BL}] \mathbf{B}_{R}^{T}.$$
(9)

Here $G_{L(R),TL}$, $G_{L(R),TR}$, $G_{L(R),BL}$, and $G_{L(R),BR}$ are the submatrices at the top-left (TL), top-right (TR), bottom-left (BL), and bottom-right (BR) corners of the Green's function matrices $G_{L(R)} = [\epsilon S_{L(R)} - H_{L(R)}]^{-1}$, respectively. The matrices $S_{L(R)}$ and $H_{L(R)}$ represent the overlap matrix and the Hamiltonian of the unit cell in the left (right) electrode, respectively. To solve Eqs. (8) and (9) in a self-consistent manner, we need initial guesses of the self-energy matrices Σ_L and Σ_R , respectively. The initial guess can be constructed from only a limited number of the generalized Bloch waves and an orthogonal complementary space [6].

Because Eqs. (8) and (9) are both solved repeatedly in a self-consistent manner, the expensive computation for the inverse matrix has to be performed many times. Therefore, the computational expenses can clearly be seen as $\mathcal{O}(N_L^3)$ for solving Eq. (8) and as $\mathcal{O}(M_R^3)$ for solving Eq. (9). According to Appendix B, the generalized Bloch wave matrices $\mathbf{Q}_{M_L(N_L)}^{\text{ref}}$ and $\mathbf{Q}_{M_R(N_R)}^{\text{tra}}$ are composed of r_L and r_R column vectors, respectively. Here $r_{L(R)} = \text{rank } \mathbf{B}_{L(R)} \ll \min(M_{L(R)}, N_{L(R)})$. This indicates that the rank number of the self-energy matrix $\mathbf{\Sigma}_{L(R)}$ is at most only $r_{L(R)}$ and that the matrices are rank deficient. It is expected that the dimensions of Eqs. (8) and (9) are reduced to r_L and r_R , respectively, so the computational expenses for solving Eq. (8) decreases to $\mathcal{O}(r_L^3)$ and that for solving Eq. (9) to $\mathcal{O}(r_R^3)$.

B. Linear-algebraic procedure to reduce computational expenses

In this subsection, we address how to reduce the computational expenses for determining the self-energy matrices Σ_L and Σ_R using a linear-algebraic procedure. Based on the singular value decomposition technique (see Appendix C), the interaction matrix $B_{L(R)}$ is decomposed into a product of three matrices:

$$\mathbf{B}_{L(R)} = \underbrace{\begin{bmatrix} \widetilde{\mathbf{U}}_{L(R)} & \widehat{\mathbf{U}}_{L(R)} \end{bmatrix}}_{\mathbf{U}_{L(R)}} \begin{bmatrix} \mathbf{0} & \mathbf{0} \\ \widehat{\mathbf{B}}_{L(R)} & \mathbf{0} \end{bmatrix} \underbrace{\begin{bmatrix} \widehat{\mathbf{V}}_{L(R)}^{T} \\ \widetilde{\mathbf{V}}_{L(R)}^{T} \end{bmatrix}}_{\mathbf{V}_{L(R)}^{T}}, \quad (10)$$

where the submatrix $\widehat{\mathbf{B}}_{L(R)}$ is square diagonal of the order $r_{L(R)}$ and composed of the singular values of the matrix $\mathbf{B}_{L(R)}$, i.e., $\widehat{\mathbf{B}}_{L(R)} = \mathrm{diag}(\sigma_{L(R),1},\sigma_{L(R),2},\ldots,\sigma_{L(R),r_{L(R)}})$ and $r_{L(R)} = \mathrm{rank}\ \mathbf{B}_{L(R)}$. The $M_{L(R)} \times r_{L(R)}$ rectangular matrix $\widehat{\mathbf{V}}_{L(R)}$ and the $N_{L(R)} \times r_{L(R)}$ rectangular matrix $\widehat{\mathbf{V}}_{L(R)}$ represent the subspaces spanned by $r_{L(R)}$ left and right singular vectors of the matrix $\mathbf{B}_{L(R)}$, respectively. The remaining matrices $\widetilde{\mathbf{U}}_{L(R)}$ and $\widetilde{\mathbf{V}}_{L(R)}$ are the orthogonal components of the subspace matrix $\widehat{\mathbf{U}}_{L(R)}$ and $\widehat{\mathbf{V}}_{L(R)}$ and $\widehat{\mathbf{V}}_{L(R)}$, respectively (for more details, see Appendix C). Note that $r_{L(R)} \ll \min(M_{L(R)}, N_{L(R)})$ holds, as discussed in Appendix B. The singular matrices \mathbf{U}_L , \mathbf{V}_L , \mathbf{U}_R , and \mathbf{V}_R are

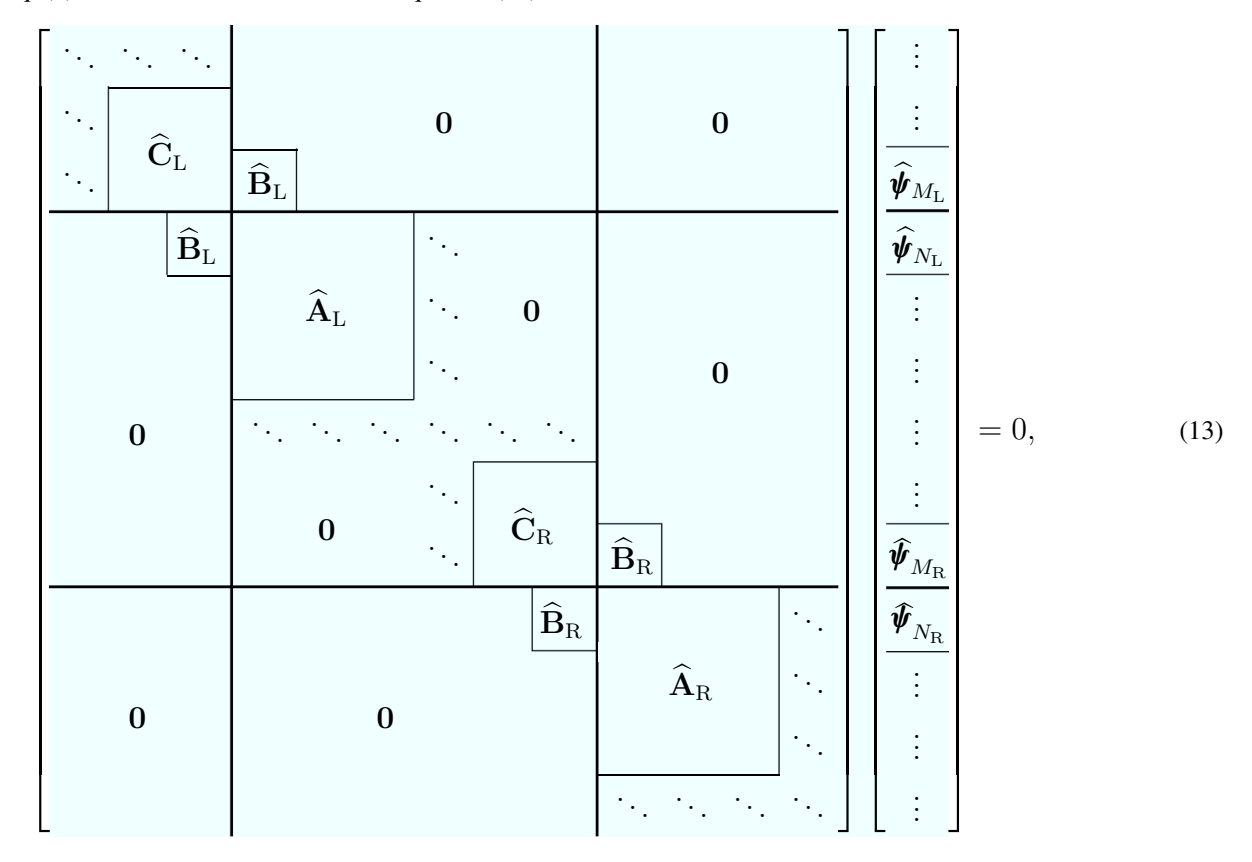
unitary of the order M_L , N_L , M_R , and N_R , respectively. We define an infinite-dimensional block-diagonal unitary matrix:

$$\mathbf{D} = \begin{bmatrix} \mathbf{I} & \mathbf{0} & & & & & & \\ \hline \mathbf{0} & \mathbf{U}_{L} & & & & & \\ & & \mathbf{V}_{L} & & \mathbf{0} & & \\ & & & \mathbf{I} & & & \mathbf{0} & \\ & & & & \mathbf{U}_{R} & & & \\ & & & & & & \\ \hline & \mathbf{0} & & \mathbf{0} & & & & \\ & & & & & & \\ \hline & \mathbf{0} & & \mathbf{0} & & & & \\ \end{bmatrix}. \tag{11}$$

Now let us consider the unitary transformation of the infinite-dimensional Kohn-Sham matrix $\mathbf{H} - \varepsilon \mathbf{S}$ with respect to the infinite-dimensional unitary matrix \mathbf{D} . The Kohn-Sham equation (1) is rewritten as

$$\mathbf{D}^{\mathrm{T}}(\mathbf{H} - \varepsilon \mathbf{S})\mathbf{D}\widehat{\boldsymbol{\psi}} = 0 \text{ and } \widehat{\boldsymbol{\psi}} = \mathbf{D}^{\mathrm{T}}\boldsymbol{\psi}. \tag{12}$$

Similarly to Eq. (2), the transformed Kohn-Sham equation (12) is described in detail, as



where $\widehat{\mathbf{C}}_{L(R)} = \mathbf{U}_{L(R)}^T \mathbf{C}_{L(R)} \mathbf{U}_{L(R)}$ and $\widehat{\mathbf{A}}_{L(R)} = \mathbf{V}_{L(R)}^T \mathbf{A}_{L(R)} \mathbf{V}_{L(R)}$. Comparing Eq. (13) with Eq. (2), one can see that the submatrices \mathbf{B}_L and \mathbf{B}_R in Eq. (2) are both reduced in dimensions and transformed into the diagonal matrices $\widehat{\mathbf{B}}_L$ and $\widehat{\mathbf{B}}_R$, respectively. Due to the reduction in the dimensions, the diagonal matrix $\widehat{\mathbf{B}}_{L(R)}$ operates only on the smaller subvectors

 $\widehat{\psi}_{N_{L(R)}}$ and $\widehat{\psi}_{M_{L(R)}}$. Note that these subvectors $\widehat{\psi}_{M_{L(R)}}$ and $\widehat{\psi}_{N_{L(R)}}$ are both composed of only $r_{L(R)}$ elements and are located to sandwich the left (right) boundary plane, as seen in Eq. (13). It should be mentioned that, although the unitary transformation deteriorates the sparseness of the diagonal blocks partitioned by the vertical and horizontal thick lines in the matrix in Eq. (2),

the deterioration of the sparseness does not affect the total computational expenses in practical calculations, as discussed below.

Because the scattering wave function vector ψ is transformed into the vector $\hat{\psi}$, as shown in Eq. (12), the open boundary conditions (3) and (4) are also transformed into

$$\widehat{\boldsymbol{\psi}}_{M_{\mathrm{L}}(N_{\mathrm{L}})} = \widehat{\boldsymbol{\phi}}_{M_{\mathrm{L}}(N_{\mathrm{L}})}^{\mathrm{in}} + \widehat{\mathbf{Q}}_{M_{\mathrm{L}}(N_{\mathrm{L}})}^{\mathrm{ref}} \boldsymbol{r}$$
 (14)

for the left electrode and into

$$\widehat{\boldsymbol{\psi}}_{M_{\mathbf{R}}(N_{\mathbf{R}})} = \widehat{\mathbf{Q}}_{M_{\mathbf{R}}(N_{\mathbf{R}})}^{\text{tra}} \boldsymbol{t} \tag{15}$$

for the right electrode, respectively. The matrices and vectors in Eqs. (3) and (4) are transformed as $\widehat{\boldsymbol{\phi}}_{M_L}^{in} = \widehat{\mathbf{U}}_L^T \boldsymbol{\phi}_{M_L}^{in}$, $\widehat{\boldsymbol{\phi}}_{N_L}^{in} = \widehat{\mathbf{V}}_L^T \boldsymbol{\phi}_{N_L}^{in}$, $\widehat{\boldsymbol{Q}}_{M_L}^{ref} = \widehat{\mathbf{U}}_L^T \mathbf{Q}_{M_L}^{ref}$, $\widehat{\mathbf{Q}}_{N_L}^{ref} = \widehat{\mathbf{V}}_L^T \mathbf{Q}_{N_L}^{ref}$, $\widehat{\mathbf{Q}}_{N_R}^{tra} = \widehat{\mathbf{U}}_R^T \mathbf{Q}_{M_R}^{tra}$, and $\widehat{\mathbf{Q}}_{N_R}^{tra} = \widehat{\mathbf{V}}_R^T \mathbf{Q}_{N_R}^{tra}$. Note that the matrices used for these transformations are not the left and right singular matrices $\mathbf{U}_{L(R)}$ and $\mathbf{V}_{L(R)}$ but the rectangular subspace matrices $\widehat{\mathbf{U}}_{L(R)}$ and $\widehat{\mathbf{V}}_{L(R)}$, which are both vertically long rectangular matrices composed of only $r_{L(R)}$ singular vectors and uniquely determined as mentioned in Appendix \mathbf{C} . According to Appendix \mathbf{B} , the matrices $\mathbf{Q}_{M_L}^{ref}$ and $\mathbf{Q}_{N_L}^{ref}$ ($\mathbf{Q}_{N_R}^{tra}$ and $\mathbf{Q}_{M_R}^{tra}$) are composed of $r_{L(R)}$ generalized Bloch wave functions of the left (right) electrode, so the transformed matrices $\widehat{\mathbf{Q}}_{M_L}^{ref}$ and $\widehat{\mathbf{Q}}_{N_L}^{ref}$ ($\widehat{\mathbf{Q}}_{N_R}^{tra}$ and $\widehat{\mathbf{Q}}_{M_R}^{tra}$) are both invertible square of the order $r_{L(R)}$.

As we have transcribed Eq. (2) into Eq. (5), using the open boundary conditions (14) and (15), the infinite-dimensional transformed Kohn-Sham equation (13) is transcribed into the following finite-dimensional linear equations, for which a transformed scattering wave function in the transition region satisfies

$$\left[\mathbf{D}_{0}^{\mathrm{T}}(\varepsilon\mathbf{S}_{0}-\mathbf{H}_{0})\mathbf{D}_{0}-\widehat{\boldsymbol{\Sigma}}_{0}\right]\begin{bmatrix}\widehat{\boldsymbol{\psi}}_{N_{\mathrm{L}}}\\\vdots\\\vdots\\\widehat{\boldsymbol{\psi}}_{M_{\mathrm{R}}}\end{bmatrix}=\begin{bmatrix}\widehat{\boldsymbol{\varphi}}\\0\\\vdots\\0\end{bmatrix},\qquad(16)$$

where $\widehat{\boldsymbol{\varphi}} = \widehat{\mathbf{B}}_L \widehat{\boldsymbol{\phi}}_{M_L}^{in} - \widehat{\boldsymbol{\Sigma}}_L \widehat{\boldsymbol{\phi}}_{N_L}^{in}$. The matrix \mathbf{D}_0 represents the submatrix present in the center of the infinite-dimensional unitary matrix \mathbf{D} shown in Eq. (11), which corresponds to the transition region. Note that the matrix \mathbf{D}_0 is also unitary. The matrix $\widehat{\boldsymbol{\Sigma}}_0$ has nonzero submatrices $\widehat{\boldsymbol{\Sigma}}_L$ and $\widehat{\boldsymbol{\Sigma}}_R$ only at the top-left and bottom-right corners. The matrices $\widehat{\boldsymbol{\Sigma}}_L$ and $\widehat{\boldsymbol{\Sigma}}_R$ represent reduced retarded self-energy operators for corresponding electrodes, and they are given by

$$\widehat{\mathbf{\Sigma}}_{L} = \widehat{\mathbf{B}}_{L} \widehat{\mathbf{Q}}_{M_{L}}^{\text{ref}} [\widehat{\mathbf{Q}}_{N_{L}}^{\text{ref}}]^{-1}$$
(17)

and

$$\widehat{\mathbf{\Sigma}}_{R} = \widehat{\mathbf{B}}_{R} \widehat{\mathbf{Q}}_{N_{R}}^{\text{tra}} [\widehat{\mathbf{Q}}_{M_{R}}^{\text{tra}}]^{-1}, \tag{18}$$

respectively. Hence, the submatrices $\widehat{\Sigma}_L$ and $\widehat{\Sigma}_R$ can clearly be seen as square of the orders r_L and r_R , respectively.

Calculating all $r_{\rm L}$ column vectors of the reduced generalized Bloch wave matrices $\widehat{\mathbf{Q}}_{M_{\rm L}}^{\rm ref}$ and $\widehat{\mathbf{Q}}_{N_{\rm L}}^{\rm ref}$ is still impractical, for the reason mentioned in the previous subsection. Therefore, Eqs. (17) and (18) are not available to calculate the self-energy matrices accurately in numerical calculations. However, following the discussion in Sec. IIB2 in Ref. [12] with respect to the matrix product $\widehat{\mathbf{Q}}_{M_{\rm L}}^{\rm ref} [\widehat{\mathbf{Q}}_{N_{\rm L}}^{\rm ref}]^{-1}$ in Eq. (17), we can derive the

TABLE I. The row dimension $M_{\rm L}$ and rank number $r_{\rm L}$ of the interaction matrix ${\bf B}_{\rm L}$, and the wall-clock time t for solving Eq. (19) for the following five systems. The wall-clock time t is measured on the supercomputer JURECA at Forschungszentrum Jülich, which is equipped with two Intel Xeon E5-2680v3 processors per a computing node. Note that the interaction matrices ${\bf B}_{\rm L}$ used here are all square, i.e., $M_{\rm L} = N_{\rm L}$.

		$M_{ m L}$	$r_{ m L}$	t (s)
Al(001) bu	8624	3264	37	
Au atomic ch	nain	9900	3614	40
C	Coarse grids	22176	8136	285
Graphene nanoribbon	Dense grids	82080	36552	_
Au(111) bu	lk	33880	9320	312ª

^aComparing to the other three benchmark tests, twice the computing resources have been used for this test.

self-consistent equation for the reduced self-energy matrix of the left electrode $\widehat{\Sigma}_L$ as

$$\widehat{\mathbf{\Sigma}}_{L} = \widehat{\mathbf{G}}_{L} [\widehat{\mathbf{G}}_{L,BR} + \widehat{\mathbf{G}}_{L,BL} [\widehat{\mathbf{\Sigma}}_{L}^{-1} - \widehat{\mathbf{G}}_{L,TL}]^{-1} \widehat{\mathbf{G}}_{L,TR}] \widehat{\mathbf{B}}_{L}. \quad (19)$$

In the same manner, with respect to the matrix product $\widehat{\mathbf{Q}}_{N_R}^{\text{tra}}[\widehat{\mathbf{Q}}_{M_R}^{\text{tra}}]^{-1}$ in Eq. (18), we can also derive the self-consistent equation for the reduced self-energy matrix of the right electrode $\widehat{\boldsymbol{\Sigma}}_R$ as

$$\widehat{\boldsymbol{\Sigma}}_{R} = \widehat{\boldsymbol{B}}_{R} [\widehat{\boldsymbol{G}}_{R,TL} + \widehat{\boldsymbol{G}}_{R,TR} [\widehat{\boldsymbol{\Sigma}}_{R}^{-1} - \widehat{\boldsymbol{G}}_{R,BR}]^{-1} \widehat{\boldsymbol{G}}_{R,BL}] \widehat{\boldsymbol{B}}_{R}. \quad (20)$$

In both equations, the matrices $\widehat{\mathbf{G}}_{X,Y}$ for Y = TL,TR,BL,BR are determined as

$$\begin{bmatrix} \widehat{\mathbf{G}}_{X,TL} & \widehat{\mathbf{G}}_{X,TR} \\ \widehat{\mathbf{G}}_{X,BL} & \widehat{\mathbf{G}}_{X,BR} \end{bmatrix} = \begin{bmatrix} \widehat{\mathbf{V}}_{X}^{T} \\ \widehat{\mathbf{U}}_{X}^{T} \end{bmatrix} \begin{bmatrix} \mathbf{G}_{X,TL} & \mathbf{G}_{X,TR} \\ \mathbf{G}_{X,BL} & \mathbf{G}_{X,BR} \end{bmatrix} \times \begin{bmatrix} \widehat{\mathbf{V}}_{X} & \widehat{\mathbf{U}}_{X} \end{bmatrix}$$
(21)

for X = L,R. Consequently, one can easily see that the matrices in Eq. (19) are all square of the order r_L , so the computational expenses for determining the reduced self-energy matrix $\widehat{\Sigma}_L$ is estimated to be $\mathcal{O}(r_L^3)$. From Eq. (20), one can also see that the computational expenses for determining the reduced self-energy matrix $\widehat{\Sigma}_R$ is estimated to be $\mathcal{O}(r_R^3)$.

From Eqs. (5), (10), and (16), the self-energy matrix $\Sigma_{L(R)}$ and the reduced self-energy matrix $\widehat{\Sigma}_{L(R)}$ are found to be associated by the following equations:

$$\Sigma_{L} = \widehat{\mathbf{V}}_{L} \widehat{\Sigma}_{L} \widehat{\mathbf{V}}_{L}^{\mathrm{T}}, \tag{22}$$

$$\mathbf{\Sigma}_{R} = \widehat{\mathbf{U}}_{R} \widehat{\mathbf{\Sigma}}_{R} \widehat{\mathbf{U}}_{R}^{T}. \tag{23}$$

In the practical calculations of scattering wave functions ψ , solving the linear equation (5) would be more reasonable than solving the linear equation (16), because the coefficient matrix in Eq. (5) is more sparse than that in Eq. (16), and Eq. (5) is more advantageous than Eq. (16) in using iterative solution techniques, such as conjugate gradient methods.

C. Comparison of computational expenses

In Table I, the row dimension M_L and rank number r_L of the interaction matrix \mathbf{B}_L , and the wall-clock time t for solving

Eq. (19), are listed for Al(001) bulk, Au atomic chain, Au(111) bulk, and graphene nano ribbon electrodes. The interaction matrices used here are all square, i.e., $M_L = N_L$. As mentioned in the previous subsections, the computational expenses in solving the self-consistent equation (8) are $\mathcal{O}(M_L^3)$, and those in solving the reduced self-consistent equation (19) are $\mathcal{O}(r_L^3)$. Therefore, one can see from Table I that the computational expenses for the five systems are reduced by more than 90%. More specifically, in the case of the Au(111) bulk, determining the self-energy matrix Σ_L by following Eq. (8) is estimated to take \sim 15,000 s. In addition to this, the memory consumption for storing the matrices is also clearly reduced by more than 80%. The same discussion can be hold for the self-consistent equations (9) and (20) for the self-energy matrix Σ_R of the semi-infinite right electrode.

To keep the sum of reflection and transmission probabilities exactly 1, both probabilities have to be accurately evaluated from the reflection and transmission coefficients of scattering wave functions. These coefficients are obviously influenced strongly by the quantities around the boundary planes, i.e., the self-energy matrices. Through controlling the convergence of the self-consistent equations (19) and (20), we can keep the sum of reflection and transmission probabilities 1 within numerical error on the order of 10^{-8} or less.

III. APPLICATIONS TO FULLERENE MOLECULAR JUNCTIONS

In this section, we present an application of the self-energy matrices obtained by the aforementioned procedure for electron transport calculations. Since Joachim et al. investigated the electron transport of a single C₆₀ fullerene molecule [39], fullerene molecules are now recognized as potentially promising materials for molecular electronics devices. So far, the C₆₀ fullerene molecule and its derivatives have been studied for their electron transport properties [26], and the smallest possible fullerene molecule C_{20} [22,23], consisting solely of pentagons, is also theoretically examined for the electron conductance by methods using localized basis sets [25]. We have theoretically investigated electron transmissions of a single C₂₀ molecule in a junction structure with a couple of jellium electrodes using the overbridging boundary matching method [24]. Although the jellium approximation brings analytically determined self-energy matrices and benefits the computational expenses very much [15,40], the oversimplification of metal electrodes is known to cause artificial and unphysical electron scattering at the interfaces between the jellium and atomistic structures [41]. Now, using the aforementioned transport calculation method, we re-evaluate the electron transport properties of C₂₀ molecular junctions comprising crystalline Al electrodes and demonstrate that relative position of the C₂₀ molecule to the electrode surface largely affects the electron transmission, which is impossible to be evaluated as long as using the uniform positive background approximation.

Figure 2 shows schematic representations of a fullerene molecular junction employed in the electron transport calculations. A single C_{20} molecule is sandwiched between the couple of semi-infinite Al(001) bulk electrodes. The separation between the Al surface layer and the nearest C atom is set to 1.42 Å (2.68 bohrs). To evaluate the fluctuation of the

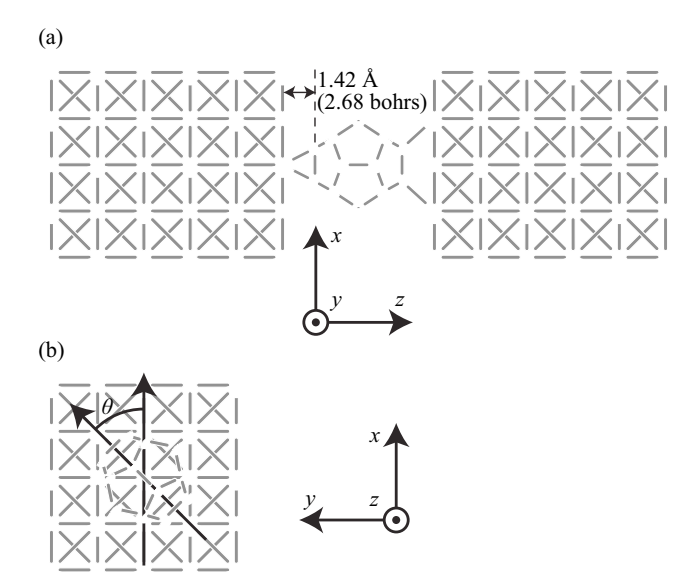


FIG. 2. Schematic representations of a C_{20} fullerene molecular junction. Panel (a) shows the side view of the molecular junction before structural optimization. The brown and blue spheres represent C and Al atoms, respectively. A C_{20} molecule is sandwiched between a couple of Al(001) bulk electrodes, so the C–C bonds close to the electrodes are parallel to the electrode surfaces. The orientation of the molecule with respect to the z axis is varied, and the angle between the x axis and the C–C bond attaching to the electrode surface is denoted by θ .

electron transmission depending on the relative position of the molecule with respect to the atomistic structure of the electrode surface, we change the orientation of the molecule. More specifically, angle θ between the x axis and the C–C bond close to the electrode surface is varied as depicted in Fig. 2(b). The geometry of the C_{20} fullerene molecule is optimized in an isolated gas phase by using the electronic structure calculation code RSPACE [13,42], which is based on the real-space finite-difference formalism. On the other hand, structural optimization of the whole junction systems is not performed in order to evaluate difference in the transport properties caused only by the difference in the molecular orientation. Here, the scattering wave function inside the transition region is determined in a non-self-consistent manner to given potentials. The effective local potential and pseudopotential parameters, being necessary for constructing the Hamiltonian of the transition region, \mathbf{H}_0 in Eq. (5), are determined under a periodic boundary condition by using the RSPACE code, in order to treat physical quantities on the same footing to the subsequent transport calculations. The pseudopotential data sets are given by projector-augmented wave method [30]. The exchange-correlation interaction is treated by the generalized gradient approximation proposed by Perdew, Burke, and Ernzerhof [43] within the framework of the density-functional theory [18]. In these calculations, it turns out that the dimensions of the left (right) interaction matrix $M_{\rm L(R)} = N_{\rm L(R)} = 8624$ and the matrix is rank-deficient with the rank of $r_{L(R)} = 3264$. Note that scattering wave functions obtained by such non-self-consistent calculations are just as correct only within a linear response regime; however, one can

TABLE II. Total and channel-decomposed electron transmissions at the Fermi energy $E_{\rm F}$ for C_{20} molecular junctions with crystalline and jellium-approximated Al electrodes. θ represents the rotation angle of the molecule with respect to the z axis and is defined in Fig. 2(b).

		Channel transmission		
$ heta^\circ$	$T_{ m total}$	T_{1st}	T_{2nd}	T_{3rd}
0	2.84	0.90	0.72	0.61
11.25	2.78	0.86	0.84	0.51
22.5	2.86	0.82	0.82	0.68
33.75	2.11	0.89	0.42	0.41
45	1.24	0.37	0.29	0.16
Jellium ^a	1.54	0.47	0.47	0.35

aReference [24].

perform more efficient computations than iterating expensive self-consistent cycles [44]. Total electron transmission $T(\varepsilon)$ is evaluated by the Landauer-Büttiker formula [45],

$$T(\varepsilon) = \sum_{i} T_{i}(\varepsilon), \tag{24}$$

where $T_i(\varepsilon)$ represents transmission probability of electrons flowing through the *i*th transmission eigenchannel and is evaluated from scattering wave functions using the channel decomposition technique [46].

In Table II, the total and channel-decomposed transmissions of the electrons injected at the Fermi energy $E_{\rm F}$, i.e., $T(E_{\rm F})$ and $T_i(E_F)$, are listed for different C-C bond angles θ and compared with those obtained for the C₂₀ molecular junction with jellium electrodes [24]. One can easily see that the electron transmissions are largely affected by the rotation angle θ . Moreover, the transmission values obtained for the fully atomistic electrodes deviate from those obtained for the jellium electrodes. The result indicates that direct attachment of structureless jellium electrode to atomistic objects may hinder us from evaluating electron transport properties correctly. This indication is reasonable from the viewpoint that, in general, the electron transmission through molecular junction is dominated by mode matching between molecular orbitals and electrode states, and the structureless jellium approximation does not reproduce the wave function modes of the corresponding crystalline electrode.

To investigate the electron transport properties more concretely, we perform structural optimization of the C_{20} molecular junction. Figure 3(a) shows the optimized structure of the C_{20} molecular junction with $\theta=0$, where all of the C_{20} molecule and the two surface layers of each electrode are relaxed and the rest fixed. As the result of the structural optimization, the electrode surface is deformed to enclose the molecule. The C_{20} molecule deforms asymmetric with respect to the xy plane crossing the center of the molecule, because the interface geometries between the molecule and the electrode surfaces are not equivalent to each other. As shown in Fig. 3(b), the total electron transmission at the Fermi energy after the structural optimization is 2.12 and smaller than that before the structural optimization, which is 2.84 as seen in Table II. In addition, comparing the channel transmissions at the Fermi

(a) Optimized geometry

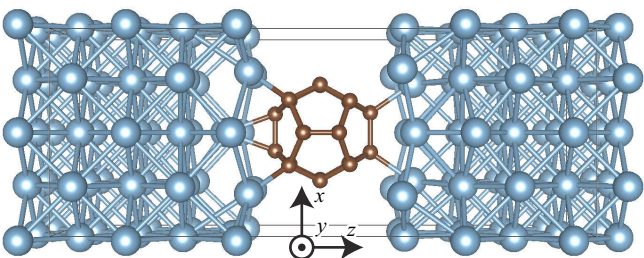


FIG. 3. Optimized geometry and electron transmission spectra of a C_{20} molecular junction after structural optimization. In (a), the blue spheres represent Al atoms, and brown ones C atoms. In (b), the total and channel-decomposed transmissions of the molecular junction are plotted by filled and open circles, respectively. $E_{\rm F}$ denotes the Fermi energy.

Energy E- E_F (eV)

level in Fig. 3(b) with those for $\theta=0$ in Table II, it is found that two transmission channels open more than 50%, while before the structural optimization three channels open more than 50%. This fact also implies that the transmission channels are sensitive to the geometrical change.

Now let us examine the transmission eigenchannels from the viewpoint of real-space pictures. Figures 4(a), 4(b), and 4(c) show the spatial distributions of the first, second, and third eigenchannels at the Fermi energy, respectively. Comparing them with the spatial distributions of the C_{20} molecular orbitals, which are calculated for the deformed C_{20} molecule in an isolated gas phase, the first, second, and third channels are found to correspond to the unoccupied molecular orbitals in Figs. 4(d), 4(g), and 4(e), respectively. In other words, these unoccupied molecular orbitals mainly contribute to the electron conduction through the molecular junction at the Fermi energy. This is reasonable from the fact that fullerene molecules are in general electronegative. Indeed, the electronic structure calculations reveal that the electronic bands resulting from the hybridization between the unoccupied molecular orbitals and the electrode states exist to cross over the Fermi energy.

IV. CONCLUSION

In this paper, we have tackled the problem of reducing the computational expenses in evaluating the self-energy matrices of semi-infinite electrodes, whose computational expenses have been proportional to cube of the matrix size. By virtue

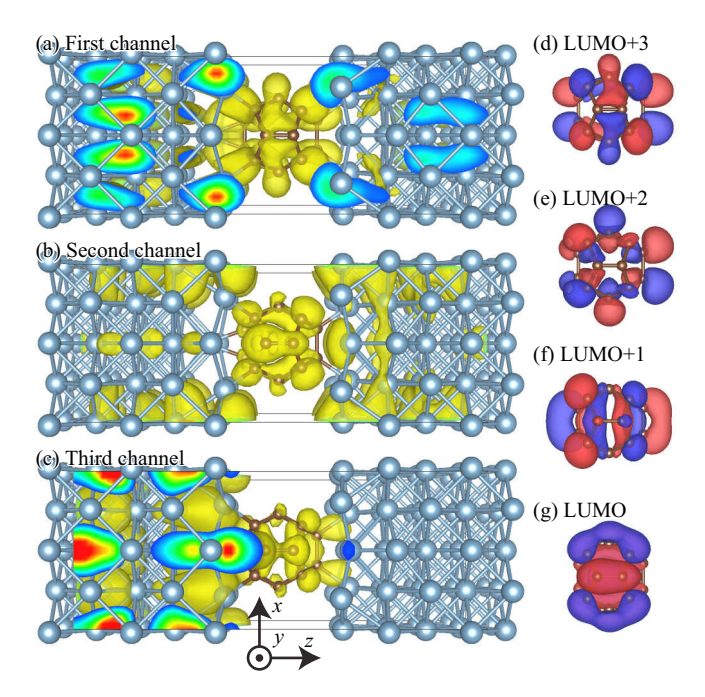


FIG. 4. Spatial distributions of the transmission channels of a C_{20} molecular junction and C_{20} molecular orbital after deformation. Panels (a), (b), and (c) exhibit the first, second, and third transmission channels of the electrons injected from the left electrode at the Fermi energy, respectively. Panels (d)–(g) show the fourth-, third-, second-, and first-lowest unoccupied molecular orbitals of the free-standing molecule, which is taken from the optimized junction structure shown in Fig. 3(a).

of the singular value decomposition, we have reduced the dimension of the self-consistent equation to be solved for the self-energy matrix, and the computational expenses are proportional to cube of the matrix rank. From practical performance tests, it is found that the computational expenses are reduced by more than 90%, and the memory space for storing the matrices is also reduced by more than 80%. We have also carried out practical electron transport calculations with the self-energy matrices obtained by the present procedure for C_{20} molecular junctions. As the results of the electron transport calculations, it has been found that the transport properties of the molecular junction are sensitive to the rotation angle of the molecule with respect to the axis perpendicular to the electrode surface. By means of the channel-decomposition technique, it turns out that some unoccupied states of the C₂₀ molecule mainly contribute to the electron conduction around the Fermi energy.

ACKNOWLEDGMENTS

This work was financially supported in part by the Core-to-Core program of Deutsche Forschungsgemeinschaft and the Japan Society for the Promotion of Science. The numerical calculations in the present work were carried out on the supercomputer JURECA at Jülich Supercomputing Centre, Forschungszentrum Jülich.

APPENDIX A: SELF-CONSISTENT EQUATION

We present the derivation of the self-consistent Eqs. (8) and (9). Note that in this section the subscripts representing the left or right electrode is omitted for simplicity. From Eq. (8) in Ref. [35], one can see that the sets of generalized Bloch wave functions in the boundary regions, $\mathbf{Q}_{i,M(N)} = \{q_{M(N),1}^i, q_{M(N),2}^i, \ldots\}$ as seen in Fig. 5, satisfy the following equations:

$$\mathbf{Q}_{i,N} = \mathbf{G}_{\mathrm{TL}} \mathbf{B}^{\mathrm{T}} \mathbf{Q}_{i-1,M} + \mathbf{G}_{\mathrm{TR}} \mathbf{B} \mathbf{Q}_{i+1,N}, \tag{A1}$$

$$\mathbf{Q}_{i,M} = \mathbf{G}_{\mathrm{BL}} \mathbf{B}^{\mathrm{T}} \mathbf{Q}_{i-1,M} + \mathbf{G}_{\mathrm{BR}} \mathbf{B} \mathbf{Q}_{i+1,N}. \tag{A2}$$

The matrix **B** represents the interaction between the neighboring unit cells of a bulk electrode system, e.g., \mathbf{B}_L in Fig. 5, and the matrix dimensions are assumed to be $M \times N$. The matrices \mathbf{G}_{TL} , \mathbf{G}_{TR} , \mathbf{G}_{BL} , and \mathbf{G}_{BR} represent the submatrices at the top-left, top-right, bottom-left, and bottom-right corners of the Green's function matrix of the truncated Hamiltonian for a unit cell of the electrode bulk system, e.g., \mathbf{H}_L in Fig. 5, and they are $N \times N$, $N \times M$, $M \times N$, and $M \times M$ in dimensions, respectively. Since the matrix product $\mathbf{BQ}_{i,N}$ is a full-rank tall matrix as discussed in Appendix B, we can define the pseudoinverse $[\mathbf{BQ}_{i,N}]^{-1}$, which satisfies $[\mathbf{BQ}_{i,N}]^{-1}\mathbf{BQ}_{i,N} = \mathbf{I}_r$. Multiplication of $[\mathbf{BQ}_{i,N}]^{-1}\mathbf{BQ}_{i,N}$ to the first term in the right-hand side of Eq. (A1) from the right leads to

$$\mathbf{Q}_{i,N} = \mathbf{G}_{\mathrm{TL}} \mathbf{B}^{\mathrm{T}} \mathbf{Q}_{i-1,M} [\mathbf{B} \mathbf{Q}_{i,N}]^{-1} \mathbf{B} \mathbf{Q}_{i,N} + \mathbf{G}_{\mathrm{TR}} \mathbf{B} \mathbf{Q}_{i+1,N}.$$
(A3)

Using the definition of the self-energy matrix of the semi-infinite left electrode, $\Sigma = \mathbf{B}^{\mathrm{T}}\mathbf{Q}_{i-1,M}[\mathbf{B}\mathbf{Q}_{i,N}]^{-1}\mathbf{B}$, which is presented as Eq. (6), the set of the generalized Bloch wave

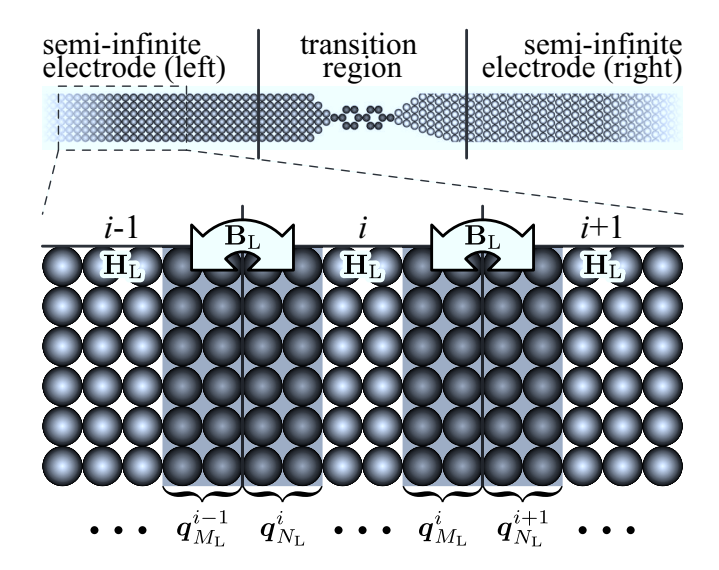


FIG. 5. Schematic representation of a bulk electrode. The matrices $\mathbf{B}_{\rm L}$ and $\mathbf{H}_{\rm L}$ represent the interaction matrix between the neighboring unit cells and the Hamiltonian matrix truncated by a unit cell, respectively. The vectors $\mathbf{q}_{M_{\rm L}}^{i-1}$, $\mathbf{q}_{N_{\rm L}}^{i}$, $\mathbf{q}_{M_{\rm L}}^{i}$, and $\mathbf{q}_{N_{\rm L}}^{i+1}$ denote the generalized Bloch wave functions in the respective boundary regions, which are represented by dark gray areas and are subject to the influence of the interaction matrix $\mathbf{B}_{\rm L}$.

functions $\mathbf{Q}_{i,N}$ is written as

$$\mathbf{Q}_{i N} = [\mathbf{I}_{N} - \mathbf{G}_{TL} \mathbf{\Sigma}]^{-1} \mathbf{G}_{TR} \mathbf{B} \mathbf{Q}_{i+1 N}. \tag{A4}$$

Similarly, by applying the relations $[\mathbf{BQ}_{i,N}]^{-1}\mathbf{BQ}_{i,N} = \mathbf{I}_r$ and $\mathbf{\Sigma} = \mathbf{B}^{\mathsf{T}}\mathbf{Q}_{i-1,M}[\mathbf{BQ}_{i,N}]^{-1}\mathbf{B}$ to Eq. (A2), the set of the generalized Bloch wave functions $\mathbf{Q}_{i,M}$ is written as

$$\mathbf{Q}_{i,M} = \mathbf{G}_{\mathrm{BL}} \mathbf{B}^{\mathrm{T}} \mathbf{Q}_{i-1,M} [\mathbf{B} \mathbf{Q}_{i,N}]^{-1} \mathbf{B} \mathbf{Q}_{i,N} + \mathbf{G}_{\mathrm{BR}} \mathbf{B} \mathbf{Q}_{i+1,N},$$
(A5)

$$= \mathbf{G}_{\mathrm{BL}} \mathbf{\Sigma} \mathbf{Q}_{i,N} + \mathbf{G}_{\mathrm{BR}} \mathbf{B} \mathbf{Q}_{i+1,N}. \tag{A6}$$

Substitution of Eq. (A4) for Eq. (A6) leads to

$$\mathbf{Q}_{i,M} = \mathbf{G}_{BR} \mathbf{B} \mathbf{Q}_{i+1,N}$$

+ $\mathbf{G}_{BL} \mathbf{\Sigma} [\mathbf{I}_N - \mathbf{G}_{TL} \mathbf{\Sigma}]^{-1} \mathbf{G}_{TR} \mathbf{B} \mathbf{Q}_{i+1,N}.$ (A7)

By multiplying $[\mathbf{B}\mathbf{Q}_{i+1,N}]^{-1}\mathbf{B}\mathbf{Q}_{i+1,N} = \mathbf{I}_r$ to the left-hand side from the right and multiplying the transpose matrix \mathbf{B}^{T} to whole the equation from the left, we obtain

$$(\mathbf{\Sigma} - \mathbf{B}^{\mathrm{T}} \mathbf{G}_{\mathrm{BR}} \mathbf{B} + \mathbf{B}^{\mathrm{T}} \mathbf{G}_{\mathrm{BL}} \mathbf{\Sigma} [\mathbf{I}_{N} - \mathbf{G}_{\mathrm{TL}} \mathbf{\Sigma}]^{-1} \mathbf{G}_{\mathrm{TR}} \mathbf{B}) \mathbf{Q}_{i+1,N}$$

$$= \mathbf{0}. \tag{A8}$$

One can easily see that the self-consistent equation for the self-energy matrix of the semi-infinite left electrode, Eq. (8), is obtained from the equation above. It is obvious that the self-consistent equaion (9) is also obtained in the same manner.

Note that the discussion in this section is independent of whether the interaction matrix $\mathbf{B}_{L(R)}$ is rank deficient or full rank. Therefore, when the interaction matrices \mathbf{B}_L and \mathbf{B}_R are assumed to be full rank, the self-consistent equations (19) and (20) are also derived from the same argument.

APPENDIX B: NUMBER OF GENERALIZED BLOCH STATES IN BULK ELECTRODES

In this section, we prove that within the framework of the real-space finite-difference formalism there exist 2r generalized Bloch states in a bulk electrode, where r denotes the rank number of the interaction matrix \mathbf{B} describing the interaction between the neighboring unit cells of a bulk electrode system, as mentioned in the previous section. According to Eqs. (11)–(13) in Ref. [35], the generalized Bloch wave function subvectors in the boundary region (see Fig. 5), q_M^{i-1} and q_N^{i+1} , satisfy the generalized eigenvalue problem

$$\begin{bmatrix} \mathbf{G}_{\mathrm{BL}}\mathbf{B}^{\mathrm{T}} & \mathbf{G}_{\mathrm{BR}}\mathbf{B} \\ \mathbf{0} & \mathbf{I}_{N} \end{bmatrix} \begin{bmatrix} \boldsymbol{q}_{M}^{i-1} \\ \boldsymbol{q}_{N}^{i+1} \end{bmatrix} = \lambda \begin{bmatrix} \mathbf{I}_{M} & \mathbf{0} \\ \mathbf{G}_{\mathrm{TL}}\mathbf{B}^{\mathrm{T}} & \mathbf{G}_{\mathrm{TR}}\mathbf{B} \end{bmatrix} \times \begin{bmatrix} \boldsymbol{q}_{M}^{i-1} \\ \boldsymbol{q}_{M}^{i+1} \end{bmatrix}, \quad (B1)$$

where the matrices G_{TL} , G_{TR} , G_{BL} , and G_{BR} represent the submatrices of the Green's function matrix, as mentioned in the previous section. The matrix $I_{M(N)}$ is the identity matrix of the order M(N).

The matrix ${\bf B}$ can be decomposed into the product of three matrices as

$$\mathbf{B} = \underbrace{\begin{bmatrix} \widetilde{\mathbf{U}} & \widehat{\mathbf{U}} \end{bmatrix}}_{\mathbf{U}} \begin{bmatrix} \mathbf{0} & \mathbf{0} \\ \widehat{\mathbf{B}} & \mathbf{0} \end{bmatrix} \underbrace{\begin{bmatrix} \widehat{\mathbf{V}}^{\mathrm{T}} \\ \widetilde{\mathbf{V}}^{\mathrm{T}} \end{bmatrix}}_{\mathbf{V}^{\mathrm{T}}}$$
(B2)

based on the singular value decomposition technique (for more detail, see Appendix \mathbb{C}). Here the singular matrices \mathbb{U} and \mathbb{V} are both unitary of the orders M and N, respectively. Therefore, the block diagonal matrix

$$\begin{bmatrix} \mathbf{U} & \mathbf{0} \\ \mathbf{0} & \mathbf{V} \end{bmatrix} \tag{B3}$$

is also unitary of the order M + N. Performing the unitary transformation of the coefficient matrices of the generalized eigenvalue problem (B1) with respect to this unitary matrix, we have the transformed generalized eigenvalue problem

$$\begin{bmatrix} \mathbf{0} & \widetilde{\mathbf{G}}_{\mathrm{BL}} \widehat{\mathbf{B}} & \widetilde{\mathbf{G}}_{\mathrm{BR}} \widehat{\mathbf{B}} & \mathbf{0} \\ \mathbf{0} & \widehat{\mathbf{G}}_{\mathrm{BL}} \widehat{\mathbf{B}} & \widehat{\mathbf{G}}_{\mathrm{BR}} \widehat{\mathbf{B}} & \mathbf{0} \\ \mathbf{0} & \mathbf{0} & \mathbf{I}_{r} & \mathbf{0} \\ \mathbf{0} & \mathbf{0} & \mathbf{I}_{N-r} \end{bmatrix} \begin{bmatrix} \widetilde{\mathbf{U}}^{\mathrm{T}} \boldsymbol{q}_{M}^{i-1} \\ \widehat{\mathbf{U}}^{\mathrm{T}} \boldsymbol{q}_{M}^{i-1} \\ \widehat{\mathbf{V}}^{\mathrm{T}} \boldsymbol{q}_{N}^{i+1} \end{bmatrix} \\ = \lambda \begin{bmatrix} \mathbf{I}_{M-r} & \mathbf{0} & \mathbf{0} & \mathbf{0} \\ \mathbf{0} & \mathbf{I}_{r} & \mathbf{0} & \mathbf{0} \\ \mathbf{0} & \widehat{\mathbf{G}}_{\mathrm{TL}} \widehat{\mathbf{B}} & \widehat{\mathbf{G}}_{\mathrm{TR}} \widehat{\mathbf{B}} & \mathbf{0} \\ \mathbf{0} & \widehat{\mathbf{G}}_{\mathrm{TL}} \widehat{\mathbf{B}} & \widehat{\mathbf{G}}_{\mathrm{TR}} \widehat{\mathbf{B}} & \mathbf{0} \end{bmatrix} \begin{bmatrix} \widetilde{\mathbf{U}}^{\mathrm{T}} \boldsymbol{q}_{M}^{i-1} \\ \widehat{\mathbf{U}}^{\mathrm{T}} \boldsymbol{q}_{M}^{i+1} \\ \widehat{\mathbf{V}}^{\mathrm{T}} \boldsymbol{q}_{N}^{i+1} \end{bmatrix}, \quad (B4)$$

where

$$\begin{bmatrix} \widetilde{\mathbf{G}}_{BL} & \widetilde{\mathbf{G}}_{BR} \\ \widehat{\mathbf{G}}_{BL} & \widehat{\mathbf{G}}_{BR} \end{bmatrix} = \begin{bmatrix} \widetilde{\mathbf{U}}^T \\ \widehat{\mathbf{U}}^T \end{bmatrix} \begin{bmatrix} \mathbf{G}_{BL} \widehat{\mathbf{V}} & \mathbf{G}_{BR} \widehat{\mathbf{U}} \end{bmatrix}$$
(B5)

and

$$\begin{bmatrix} \widehat{\mathbf{G}}_{TL} & \widehat{\mathbf{G}}_{TR} \\ \widetilde{\mathbf{G}}_{TL} & \widetilde{\mathbf{G}}_{TR} \end{bmatrix} = \begin{bmatrix} \widehat{\mathbf{V}}^T \\ \widetilde{\mathbf{V}}^T \end{bmatrix} \begin{bmatrix} \mathbf{G}_{TL} \widehat{\mathbf{V}} & \mathbf{G}_{TR} \widehat{\mathbf{U}} \end{bmatrix}. \tag{B6}$$

Let us partition the generalized eigenvalue problem (B4) into three block rows as indicated by the horizontal lines therein. It is easily seen that the middle block row is a 2r-dimensional generalized eigenvalue problem and identical to the reduced generalized eigenvalue problem for the generalized Bloch wave functions presented as Eqs. (32)– (34) in Ref. [35]. The coefficient matrices of the generalized eigenvalue problem are both full rank, and, therefore, the generalized eigenvalue problem has 2r nontrivial solutions. The upper and lower block rows of Eq. (B4) are essentially identical to the upper and lower half rows of the middle block row, respectively. Consequently, the generalized eigenvalue problem (B1) has 2r nontrivial solutions of generalized Bloch states. Note that the half of the generalized Bloch waves propagate or decay rightward, and the other half leftward. According to the discussion in Ref. [35], the rank number r is much smaller than the dimensions of the interaction matrix **B**, i.e., $r \ll \min(M, N)$ in electron transport calculations using the real-space finite-difference formalism and the projector-augmented wave pseudopotentials.

APPENDIX C: SINGULAR VALUE DECOMPOSITION

The matrix decomposition introduced in Eqs. (10) and (B2) is straightforwardly derived from the general definition of the singular value decomposition of a general $M \times N$ rectangular

matrix A [47–49], i.e.,

$$\mathbf{A} = \underbrace{\begin{bmatrix} \widehat{\mathbf{U}} & \widetilde{\mathbf{U}} \end{bmatrix}}_{\mathbf{U}} \begin{bmatrix} \widehat{\mathbf{A}} & \mathbf{0} \\ \mathbf{0} & \mathbf{0} \end{bmatrix} \underbrace{\begin{bmatrix} \widehat{\mathbf{V}}^{\mathrm{T}} \\ \widetilde{\mathbf{V}}^{\mathrm{T}} \end{bmatrix}}_{\mathbf{V}^{\mathrm{T}}}, \tag{C1}$$

by swapping the matrices $\widehat{\mathbf{U}}$ and $\widehat{\mathbf{U}}$ and by swapping the upper and lower block rows of the second matrix in the right-hand side. The submatrix $\widehat{\mathbf{A}}$ represents a square diagonal matrix of the order r and is composed of the singular values of the matrix \mathbf{A} , i.e., $\widehat{\mathbf{A}} = \operatorname{diag}(\sigma_1, \sigma_2, \dots, \sigma_r)$. Note that $r = \operatorname{rank} \mathbf{A} \leq \min(M, N)$ and the singular values are positive

and in the descending order $\sigma_1 \geqslant \sigma_2 \geqslant \cdots \geqslant \sigma_r > 0$. The left and right singular matrices, \mathbf{U} and \mathbf{V} , are both unitary of the orders M and N, respectively. Each unitary matrix can be divided into two orthogonal subspaces as seen in Eq. (C1). The subspace spanned by the first r column vectors $\widehat{\mathbf{U}}$ ($\widehat{\mathbf{V}}$) is called a column (row) space and uniquely determined, while the other spanned by the rest column vectors $\widehat{\mathbf{U}}$ ($\widehat{\mathbf{V}}$) is called a left-null (null) space and underspecified. Note that the underspecified left-null and null spaces, $\widehat{\mathbf{U}}$ and $\widehat{\mathbf{V}}$, are never referred to in practical computations using the present procedure.

- Y. V. Nazarov and Y. M. Blanter, *Quantum Transport: Introduction to Nanoscience* (Cambridge University Press, Cambridge, 2009).
- [2] S. M. Lindsay, *Introduction to Nanoscience* (Oxford University Press, Oxford, 2009).
- [3] M. Di Ventra, *Electron Transport in Nanoscale Systems* (Cambridge University Press, Cambridge, 2008).
- [4] S. Datta, Electronic Transport in Mesoscopic Systems, edited by H. Ahme, M. Pepper, and A. Broers, Cambridge Studies in Semiconductor Physics and Microelectronic Engineering, Vol. 3 (Cambridge University Press, Cambridge, 1995).
- [5] P. Sautet and C. Joachim, Phys. Rev. B 38, 12238 (1988); J. Stein and C. Joachim, J. Phys. A: Mat. Gen. 20, 2849 (1987).
- [6] T. Ono and S. Tsukamoto, Phys. Rev. B 93, 045421 (2016).
- [7] T. Ono, Y. Egami, and K. Hirose, Phys. Rev. B 86, 195406 (2012).
- [8] M. Brandbyge, J.-L. Mozos, P. Ordejón, J. Taylor, and K. Stokbro, Phys. Rev. B 65, 165401 (2002); S. Sanvito, C. J. Lambert, J. H. Jefferson, and A. M. Bratkovsky, *ibid.* 59, 11936 (1999); J. Taylor, H. Guo, and J. Wang, *ibid.* 63, 245407 (2001); Y. Xue, S. Datta, and M. A. Ratner, Chem. Phys. 281, 151 (2002); J. Enkovaara, C. Rostgaard, J. J. Mortensen, J. Chen, M. Dułak, L. Ferrighi, J. Gavnholt, C. Glinsvad, V. Haikola, H. A. Hansen, H. H. Kristoffersen, M. Kuisma, A. H. Larsen, L. Lehtovaara, M. Ljungberg, O. Lopez-Acevedo, P. G. Moses, J. Ojanen, T. Olsen, V. Petzold, N. A. Romero, J. Stausholm-Møller, M. Strange, G. A. Tritsaris, M. Vanin, M. Walter, B. Hammer, H. Häkkinen, G. K. H. Madsen, R. M. Nieminen, J. K. Nørskov, M. Puska, T. T. Rantala, J. Schiøtz, K. S. Thygesen, and K. W. Jacobsen, J. Phys.: Condens. Matter 22, 253202 (2010).
- [9] K. S. Thygesen and A. Rubio, Phys. Rev. B 77, 115333 (2008);
 M. Strange, C. Rostgaard, H. Häkkinen, and K. S. Thygesen, *ibid.* 83, 115108 (2011).
- [10] M. Tsukada, K. Tagami, K. Hirose, and N. Kobayashi, J. Phys. Soc. Jpn. 74, 1079 (2005); K. Hirose, N. Kobayashi, and M. Tsukada, Phys. Rev. B 69, 245412 (2004); K. Hirose and M. Tsukada, *ibid.* 51, 5278 (1995).
- [11] T. Ono, S. Tsukamoto, Y. Egami, and Y. Fujimoto, J. Phys.: Condens. Matter 23, 394203 (2011); P. A. Khomyakov, G. Brocks, V. Karpan, M. Zwierzycki, and P. J. Kelly, Phys. Rev. B 72, 035450 (2005); P. A. Khomyakov and G. Brocks, *ibid.* 70, 195402 (2004).
- [12] Y. Fujimoto and K. Hirose, Phys. Rev. B 67, 195315 (2003).

- [13] K. Hirose, T. Ono, Y. Fujimoto, and S. Tsukamoto, *First-Principles Calculations in Real-Space Formalism* (Imperial College Press, London, 2005).
- [14] L. Kong, M. L. Tiago, and J. R. Chelikowsky, Phys. Rev. B 73, 195118 (2006).
- [15] Y. Egami, K. Hirose, and T. Ono, Phys. Rev. E 82, 056706 (2010).
- [16] Y. Egami, S. Iwase, S. Tsukamoto, T. Ono, and K. Hirose, Phys. Rev. E 92, 033301 (2015); S. Tsukamoto, Y. Egami, K. Hirose, and S. Blügel, Phys. Rev. B 84, 115443 (2011); N. Kobayashi, M. Aono, and M. Tsukada, *ibid*. 64, 121402 (2001); N. D. Lang, *ibid*. 52, 5335 (1995).
- [17] K. S. Thygesen, M. V. Bollinger, and K. W. Jacobsen, Phys. Rev. B 67, 115404 (2003).
- [18] P. Hohenberg and W. Kohn, Phys. Rev. 136, B864 (1964).
- [19] This word should not be confused with the other "self-energy" used in the methods solving many-body problems, for instance, in the *GW* approximation. Indeed, there already exist some studies to combine the *GW* approximation with electron transport calculations [9], and in these studies the word "self-energy" is separately used as "coupling or electrode self-energy" and "*GW* self-energy." For detailed description on the "self-energy" in this paper, see pp. 145–148 in Ref. 4.
- [20] Hans Henrik B. Sørensen, P. C. Hansen, D. E. Petersen, S. Skelboe, and K. Stokbro, Phys. Rev. B 77, 155301 (2008).
- [21] Hans Henrik B. Sørensen, P. C. Hansen, D. E. Petersen, S. Skelboe, and K. Stokbro, Phys. Rev. B 79, 205322 (2009).
- [22] P. Mélinon and B. Masenelli, From Small Fullerenes to Superlattices: Science and Applications (Pan Stanford, Singapore, 2012).
- [23] Y. Jin, A. Perera, V. F. Lotrich, and R. J. Bartlett, Chem. Phys. Lett. 629, 76 (2015); B. L. Zhang, C. Z. Wang, K. M. Ho, C. H. Xu, and C. T. Chan, J. Chem. Phys. 97, 5007 (1992); H. Prinzbach, A. Weiler, P. Landenberger, F. Wahl, J. Wörth, L. T. Scott, M. Gelmont, D. Olevano, and B. v. Issendorff, Nature (London) 407, 60 (2000).
- [24] M. Otani, T. Ono, and K. Hirose, Phys. Rev. B 69, 121408 (2004).
- [25] Y.-P. An, C.-L. Yang, M.-S. Wang, X.-G. Ma, and D.-H. Wang, J. Chem. Phys. 131, 024311 (2009); L. H. Wang, Y. Guo, C. F. Tian, X. P. Song, and B. J. Ding, J. Appl. Phys. 107, 103702 (2010); C. Roland, B. Larade, J. Taylor, and H. Guo, Phys. Rev. B 65, 041401 (2001).

- [26] T. Ono and K. Hirose, Phys. Rev. Lett. 98, 026804 (2007); T. Ono and S. Tsukamoto, Phys. Rev. B 84, 165410 (2011); S. Bilan, L. A. Zotti, F. Pauly, and J. C. Cuevas, *ibid.* 85, 205403 (2012); D. A. Lovey and R. H. Romero, J. Appl. Phys. 114, 144305 (2013); S. Tsukamoto and T. Nakayama, J. Chem. Phys. 122, 074702 (2005); G. Géranton, C. Seiler, A. Bagrets, L. Venkataraman, and F. Evers, *ibid.* 139, 234701 (2013); S. Yuan, S. Wang, Q. Mei, Q. Ling, L. Wang, and W. Huang, J. Phys. Chem. C 118, 617 (2014).
- [27] The Kohn-Sham orbital function ψ and the eigenvalue ε can be used as the initial guesses for the self-consistent procedure to determine the Green's function including the many-body correlation effects, i.e., information on the excited states of the system, and such the study involving the GW approximation into electron transport calculation method based on the nonequilibrium Green's function formalism has already been carried out [9].
- [28] R. G. Parr and W. Yang, *Density-Functional Theory of Atoms and Molecules* (Oxford University Press, New York, NY, 1989), Chap. 7, pp. 142–168.
- [29] W. Kohn, Rev. Mod. Phys. 71, 1253 (1999); W. Kohn and L. J. Sham, Phys. Rev. 140, A1133 (1965).
- [30] P. E. Blöchl, Phys. Rev. B **50**, 17953 (1994); G. Kresse and D. Joubert, *ibid*. **59**, 1758 (1999).
- [31] D. Vanderbilt, Phys. Rev. B 41, 7892 (1990).
- [32] N. Troullier and J. L. Martins, Phys. Rev. B 43, 1993 (1991);
 Solid State Commun. 74, 613 (1990); L. Kleinman and D. M. Bylander, Phys. Rev. Lett. 48, 1425 (1982).
- [33] J. R. Chelikowsky, N. Troullier, K. Wu, and Y. Saad, Phys. Rev. B 50, 11355 (1994); J. R. Chelikowsky, N. Troullier, and Y. Saad, Phys. Rev. Lett. 72, 1240 (1994).
- [34] When using a higher finite-difference approximation order $N_{\rm f}$ such that the matrix bandwidth of the kinetic term is larger than that of the semilocal potential term, the rank deficiency of the interaction matrix $\mathbf{B}_{\rm L(R)}$ can be avoided. However, this is not an essential solution to the mathematical problem that we discuss in this paper.
- [35] S. Tsukamoto, K. Hirose, and S. Blügel, Phys. Rev. E 90, 013306 (2014).
- [36] These general expressions of the self-energies can be derived from the definition, $\Sigma_L = \mathbf{B}_L^T \mathbf{g}_L \mathbf{B}_L$ and $\Sigma_L = \mathbf{B}_R \mathbf{g}_R \mathbf{B}_R^T$, where

- $\mathbf{g}_{L(R)}$ is the surface Green function matrix of the semi-infinite left (right) electrode. When the matrix $\mathbf{B}_{L(R)}$ is full-rank and invertible, $\mathbf{\Sigma}_L = \mathbf{B}_L^T \mathbf{Q}_{M_L}^{ref} [\mathbf{Q}_{N_L}^{ref}]^{-1}$ ($\mathbf{\Sigma}_R = \mathbf{B}_R \mathbf{Q}_{N_R}^{tra} [\mathbf{Q}_{M_R}^{tra}]^{-1}$), as presented in Refs. [14] and [15].
- [37] K. B. Petersen and M. S. Pedersen, The Matrix Cookbook (2012), http://www2.imm.dtu.dk/pubdb/p.php?3274.
- [38] D. A. Harville, *Matrix Algebra from a Statistician's Perspective* (Springer-Verlag, New York, 1997), Chap. 20, pp. 497–519.
- [39] C. Joachim, J. K. Gimzewski, R. R. Schlittler, and C. Chavy, Phys. Rev. Lett. 74, 2102 (1995).
- [40] S. Tsukamoto, V. Caciuc, N. Atodiresei, and S. Blügel, Phys. Rev. B 85, 245435 (2012); H. Kusaka and N. Kobayashi, Appl. Surf. Sci. 258, 1985 (2012); P. Song, P. Nordlander, and S. Gao, J. Chem. Phys. 134, 074701 (2011); Y. Egami, S. Aiba, K. Hirose, and T. Ono, J. Phys.: Condens. Matter 19, 365201 (2007); Y. Egami and K. Yamada, Comput. Phys. Commun. 182, 103 (2011).
- [41] J. Prasongkit, A. Grigoriev, G. Wendin, and R. Ahuja, Phys. Rev. B 81, 115404 (2010); K. Kobayashi, *ibid.* 53, 11091 (1996).
- [42] T. Ono and K. Hirose, Phys. Rev. B 72, 085115 (2005); T. Ono, M. Heide, N. Atodiresei, P. Baumeister, S. Tsukamoto, and S. Blügel, *ibid.* 82, 205115 (2010).
- [43] J. P. Perdew, K. Burke, and M. Ernzerhof, Phys. Rev. Lett. 77, 3865 (1996); 78, 1396 (1997).
- [44] L. Kong, J. R. Chelikowsky, J. B. Neaton, and S. G. Louie, Phys. Rev. B 76, 235422 (2007).
- [45] M. Büttiker, Y. Imry, R. Landauer, and S. Pinhas, Phys. Rev. B 31, 6207 (1985).
- [46] N. Kobayashi, M. Brandbyge, and M. Tsukada, Phys. Rev. B 62, 8430 (2000); M. Brandbyge, M. R. Sørensen, and K. W. Jacobsen, *ibid.* 56, 14956 (1997); N. Kobayashi and M. Tsukada, Jpn. J. Appl. Phys. 38, 3805 (1999).
- [47] W. H. Press, S. A. Teukolsky, W. T. Vetterling, and B. P. Flannery, *Numerical Recipes: The Art of Scientific Computing*, 3rd ed. (Cambridge University Press, New York, 2007).
- [48] A. K. Cline and I. S. Dhillon, in *Handbook of Linear Algebra*, Discrete Mathematics and Its Applications, edited by L. Hogben (Chapman & Hall/CRC, Boca Raton, FL, 2006) Chap. 45, pp. 45.1–45.13.
- [49] G. Golub and C. Reinsch, Numer. Math. 14, 403 (1970).